Terahertz detection by epitaxial-graphene field-effect-transistors on silicon carbide

F. Bianco, D. Perenzoni, D. Convertino, S. L. De Bonis, D. Spirito, M. Perenzoni, C. Coletti, M. S. Vitiello, and A. Tredicucci

---

Articles you may be interested in

Terahertz bolometric detection by thermal noise in graphene field effect transistor
Appl. Phys. Lett. **107**, 083506 (2015); 10.1063/1.4929768

Unipolar behavior in graphene-channel field-effect-transistors with n-type doped SiC source/drain regions
Appl. Phys. Lett. **103**, 223503 (2013); 10.1063/1.4833755

Photocurrent-based detection of terahertz radiation in graphene
Appl. Phys. Lett. **103**, 211120 (2013); 10.1063/1.4831682

Plasmonic and bolometric terahertz detection by graphene field-effect transistor
Appl. Phys. Lett. **103**, 181114 (2013); 10.1063/1.4826139

High-responsivity terahertz detection by on-chip InGaAs/GaAs field-effect-transistor array
Appl. Phys. Lett. **98**, 153504 (2011); 10.1063/1.3573825

Terahertz detection by epitaxial-graphene field-effect-transistors on silicon carbide

F. Bianco,[1,a)] D. Perenzoni,[2] D. Convertino,[3] S. L. De Bonis,[1,b)] D. Spirito,[1,c)] M. Perenzoni,[2] C. Coletti,[3] M. S. Vitiello,[1] and A. Tredicucci[2,4]

[1]NEST, Istituto Nanoscienze-CNR and Scuola Normale Superiore, Piazza S. Silvestro 12, 56127 Pisa, Italy
[2]Fondazione Bruno Kessler (FBK), Via Sommarive 18, 38123 Povo, Trento, Italy
[3]CNI@NEST, Istituto Italiano di Tecnologia, Piazza S. Silvestro 12, 56127 Pisa, Italy
[4]NEST, Istituto Nanoscienze-CNR and Dipartimento di Fisica "E. Fermi", Università di Pisa, Largo Bruno Pontecorvo 3, 56127 Pisa, Italy

We report on room temperature detection of terahertz radiation by means of antenna-coupled field effect transistors (FETs) fabricated using epitaxial graphene grown on silicon carbide. The achieved photoresponsivity ($\sim$0.25 V/W) and noise equivalent power ($\sim$80 nW/$\sqrt{\text{Hz}}$) result from the combined effect of two independent detection mechanisms: over-damped plasma wave rectification and thermoelectric effects, the latter ascribed to the presence of carrier density junctions along the FET channel. The calculated plasmonic and thermoelectric response reproduces qualitatively well the measured photovoltages; the experimentally observed sign-switch demonstrates the stronger contribution of plasmonic detection compared to the thermoelectric one. These results unveil the potential of plasmonic detectors exploiting epitaxial graphene on silicon carbide for fast large area imaging of macroscopic samples. © 2015 AIP Publishing LLC.
[http://dx.doi.org/10.1063/1.4932091]

Among the variety of active and passive photonic devices[1,2] for the generation[3–5] and manipulation[6–9] of terahertz (THz) radiation, graphene has proven to be an ideal material for low-cost room-temperature (RT) photodetection systems.[1,10] Generally, photodetection is based on the conversion of incoming photons into an electrical signal. In the THz frequency range, this conversion can be achieved in room-temperature graphene via three main mechanisms: bolometric (associated to graphene channel conductivity variation due to photon absorption),[11,12] thermoelectric (TE) (related to a photovoltage generated by a temperature gradient within the graphene channel),[13] and plasmonic (due to rectification of the THz-induced ac current in the channel of a graphene field effect transistor (GFET)).[14–18]

The large interest in reliable fast RT photodetection is motivated by the growing applications of THz light in areas like industrial process monitoring, biomedical diagnostics, and security controls. For imaging applications, particular attention is currently devoted to the development of sensitive, compact, portable, very fast (>GHz) imagers. RT detector arrays have been demonstrated with silicon CMOS[19] (hundred μs response time), pyroelectric,[20] or microbolometric[21] (response time in the millisecond range) detector arrays. These detectors exhibit responsivities of the order of a few kV/W and noise-equivalent-powers (NEP) < nW/$\sqrt{\text{Hz}}$. In this context, the atomic-scale thickness and the large length scalability of the channel, combined with the extremely high carrier mobility of graphene sheets, make GFETs ideal candidates for superior electronic performances[22,23] and the development of focal plane sensors with high responsivity and ultrafast response time.

In order to assemble closely spaced GFET-detector elements, large area graphene is needed. Recently, THz detection by chemical vapor deposition (CVD) graphene-FETs has been successfully reported.[17] However, graphene films CVD-grown on an insulating substrate (like the one mostly used for transistors fabrication) are currently limited to discontinuous nanometer-sized islands.[24] While CVD growth on copper foils is rapidly emerging as a powerful technique to obtain millimeter-sized single crystal graphene,[25] a high-fidelity transfer process is needed to maintain good crystalline integrity, long-distance continuity, and absence of cracks. The direct growth of graphene on the device substrate is, therefore, highly desirable. Epitaxial graphene (EG) represents a promising alternative: thanks to the graphitization of silicon carbide (SiC) by silicon (Si) sublimation, high quality graphene films can be directly grown on insulating SiC substrates in the form of large-diameter wafers.

In this letter, we report on RT THz detection with an antenna-coupled FETs exploiting epitaxial graphene grown on the Si-face of a SiC substrate (EGFET). The recorded photo-induced voltage was generated by the combination of plasma wave rectification and photothermoelectric effect across the FET channel.

The FET was obtained from bilayer graphene grown on a semi-insulating, nominally on-axis-oriented, 4 H-SiC(0001) substrate using a resistively heated cold wall reactor (BM, Aixtron).[26] Growth was performed at a temperature of 1390 °C and a pressure of 780 mbar for 20 min. Assessment of the distribution of the number of layers was conducted via spatially resolved Raman spectroscopy using a Renishaw InVia system equipped with a 532 nm laser.[25]

a)Author to whom correspondence should be addressed. Electronic mail: federicabianco82@gmail.com
b)Present address: ICFO, Av. Carl Friedrich Gauss, Centre d'Investigació en Nanociència, Castelldefels, Barcelona 08860, Spain.
c)Present address: Istituto Italiano di Tecnologia, Nanochemistry department and Graphene labs, Via Morego 30, 16163 Genova, Italy.

The graphene sheet was also characterized by atomic force microscopy (AFM). AFM micrographs showed the typical step-terrace structure of the graphitized SiC surface (Fig. 1(a)) and the presence of graphene with different thicknesses within the terrace. The correlation of the AFM image with the two-dimensional spatial distribution of the width of the 2D Raman peak (Fig. 1(b)) revealed the bilayer character of the graphene[27] on the terraces together with the presence of trilayer inclusions, typically located at the terrace edges, as in Ref. 28.

The devices consisted of a log-periodic circular-toothed antenna (see inset of Fig. 2(a)), whose lobes were connected to the source and gate of the EGFET, while the drain was a metal line. The 2.5 μm long and 2 μm wide channel was defined by etching the large area graphene through a poly-methyl methacrylate mask via oxygen/argon reactive-ion etching. Antenna and metal contacts were patterned by electron beam lithography, followed by thermal evaporation of 5 nm/100 nm chromium/gold. A 35 nm-thick hafnium oxide layer was deposited by atomic layer deposition as gate dielectric for a top-gate configuration; this corresponds to a gate-to-channel capacitance per unit area of 3.5×10^{-7} F/cm^2. The length of the gate (L_g) was 300 nm.

The detector was electrically characterized measuring the source/drain current as a function of gate voltage (V_g) while keeping source/drain voltage (V_{sd}) at 1 mV. The source/drain resistance (R_{sd}) varied from 14 to 17.5 kΩ (black curve in Fig. 1(c)) with a maximum at a gate voltage $V_{CNP} \approx 0.1$ V (charge neutrality point (CNP)). The observed p-doping can be ascribed to extrinsic contaminations (e.g., exposure to air and residual fabrication impurities), contrary to the intrinsic electron-doping reported in as-growth epitaxial graphene on SiC due to the charged dangling bonds of the buffer layer.[29] Moreover, no evident signatures of band gap opening, typical of bilayer graphene,[30] was observed in the R_{sd} curve. Tentatively, we ascribed this feature to the large fluctuating disorder potential[31,32] and/or to the superposition

FIG. 2. (a) Photovoltage as a function of the incident radiation frequency measured at $V_g = 1.2$ V, $V_{sd} = 0$ mV and for polarization at 0° and 90° with respect to the antenna axis. The data are not corrected by the spectral dependence of the source output power. The inset shows the optical image of the device. (b) Photovoltage measured as a function of the gate voltage at 263 GHz (magenta line), 295 GHz (blue line), 325 GHz (green line), and 353 GHz (red line) with $V_{sd} = 0$ mV and polarization at 0°. The ΔU shift at the CNP voltage from the 0 value is indicated for each photoresponse curve by arrow-dashed lines. The dashed vertical and horizontal lines indicate the CNP and $\Delta U = 0$ V, respectively.

of the band structures of the bilayer with the residual amounts of trilayer graphene,[28] which likely masked the presence of the band gap. The mobility and residual carrier density values were extracted by fitting the transconductance characteristic,[16] resulting in $\mu = 120$ cm^2/Vs and $n_o = 1.7 \times 10^{12}$ cm^{-2} in agreement with the typical values reported for epitaxial bilayer graphene.[33] Generally, the mobility in epitaxial graphene grown on Si-terminated SiC substrates is limited by the presence of the interfacial layer,[29] which causes Coulomb scattering as well as optical and low-energy phonon scattering,[34,35] and by short-range scattering due to structural defects, step edges and thickness inhomogeneities.[36] On the other hand, in bilayer graphene, the mobility shows a very weak temperature dependence; thus, electronic transport can be considered dominated by Coulomb and short range scattering mechanisms.[33,37]

With this basic characterization, we can estimate the expected response for the THz-induced rectification mechanism. Plasma waves are excited in the FET channel,[14,18] but, in the low frequency ($2\pi\nu\tau \ll 1$, ν being the radiation frequency and τ the carrier momentum relaxation time) and long gate regime (gate length much longer than the plasma decay length), only overdamped waves are excited, meaning that they decay before reaching the drain electrode. According to the hydrodynamic approach proposed by Dyakonov and Shur (DS),[14] the induced ac current can exist only up to a distance l_{pl} from the source. This distance is quantified as $l_{pl} = s\sqrt{\tau/\pi\nu}$, where s is the plasma wave velocity ($s \sim 10^6$ m/s[18]), $\tau \sim \mu m^*/e$ is the scattering time, $m^* = 0.028 m_e$ is the effective mass of bilayer graphene,[38] m_e is the free electron mass, e is the electron charge, and μ is the carrier mobility. Considering the mobility extracted from the FET resistance, τ becomes ~ 2 fs, so that $2\pi\nu\tau \sim 0.003$ and the decay length $l_{pl} \sim 115$ nm $< L_g$. This means that plasma wave-assisted detection in the broadband over-damped regime is expected in our detector. The detection mechanism is activated by the simultaneous modulation of the carrier density and drift velocity at the incoming
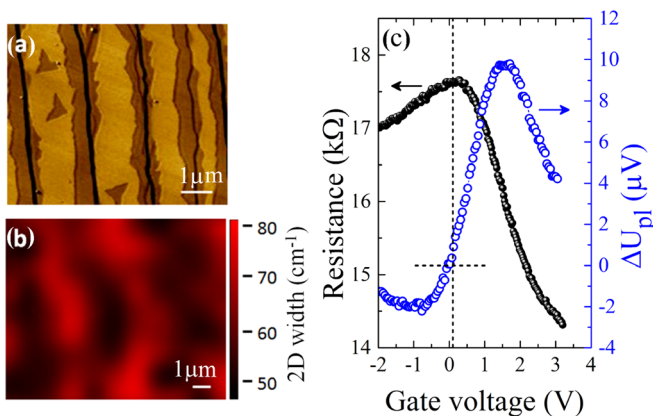

FIG. 1. Tapping-mode AFM phase signal (a) and Raman map of the 2D peak width (b) of graphene grown on SiC. The 2D peak width shows a bilayer character (black areas in Fig. 1(b)) on the terraces (light brown areas in Fig. 1(a)) and trilayer inclusions (dark brown areas in Fig. 1(a) and red areas in Fig. 1(b)) in the proximity of the SiC step. (c) Black dotted curve is the source/drain resistance measured as a function of the gate voltage with $V_{sd} = 1$ mV. Blue empty-dotted curve is the plasmonic photovoltage for overdamped plasma waves-assisted detection. The dashed vertical and horizontal lines indicate the CNP and $\Delta U = 0$ V, respectively.

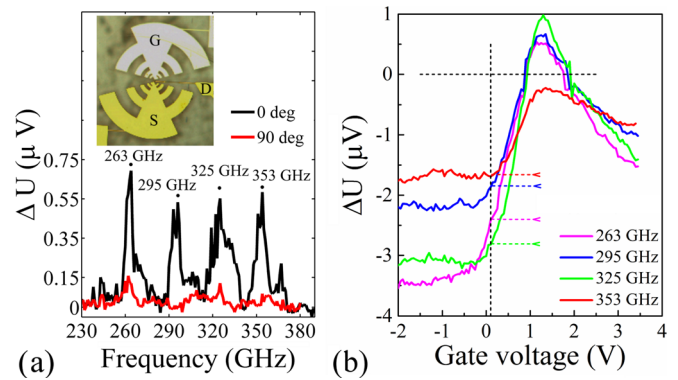radiation frequency ν. Hence, the detector photoresponse is a dc signal proportional to the incident power.

The photoresponsivity was characterized by illuminating the detector with a broadband THz source (WR2.8AMC, Virginia Diodes Inc.) covering a spectral range from 230 GHz to 375 GHz. The frequency dependent output power ranged from 0.5 mW to 1 mW (calibrated after the focusing lens). The source was modulated at 858 Hz with a fixed horizontal polarization. The variation of the polarization direction was achieved by rotating the sample. A polished Tsurupica lens was employed to focus the radiation and maximize the illumination of the detecting region. The photovoltage signal was then recorded by means of a lock-in amplifier (Signal Recovery mo. 7265 DSP) with an input impedance of 10 MΩ and variable internal gain.

Figure 2(a) shows the photovoltage (ΔU) measured as a function of the incident radiation frequency for beam polarization parallel (0°) and orthogonal (90°) to the antenna axis, while keeping $V_g = 1.2$ V and $V_{sd} = 0$ mV. As expected from the dipole antenna operation, a polarization-sensitive signal was observed: the maximum photovoltage was recorded when the polarization was parallel to the antenna axis. The frequency dependent ΔU exhibited a series of pronounced peaks, in accordance with the antenna geometry. Instead, net photovoltage suppression occurred when the radiation was cross-polarized. In fact, only a clear but weak feature was recognizable at 263 GHz.

Fixing the THz wave polarization at 0°, the photo-induced voltage was measured at the peak frequencies of Fig. 2(a) (i.e., 263 GHz, 295 GHz, 325 GHz, and 353 GHz) by sweeping the gate voltage from negative to positive values (Fig. 2(b)). All curves ($\Delta U \equiv \Delta U_{exp}$) show nearly constant negative values at negative gate voltage, while an inverted V-shape reaching small positive values at the peak is observed for positive gate voltage. In the overdamped plasma wave regime, the solution of both Eulero equation (for the drift velocity) and continuity equation (for the carrier density)[14] predicts that the plasmonic photovoltage is functionally dependent on the gate voltage according to the relation $\Delta U_{pl} = C\,\sigma^{-1}d\sigma/dV_g$. Here, σ is the source/drain conductance and C is the constant that takes into account the efficiency of the antenna coupling and the FET impedance. The blue curve in Fig. 1(c) shows ΔU_{pl} calculated as a function of the gate voltage by using the measured FET conductance and assuming $C \sim 10^{-4}$ V^2, as estimated in similar GFET detectors.[16] By comparing the trend of ΔU_{exp} with ΔU_{pl}, a general similarity between the curves was found, suggesting a detection mechanism based on the DS model. Nevertheless, the model did not comprehensively describe the detector photoresponse. In fact, contrarily to what predicted in ΔU_{pl}, a clear change of the photovoltages sign when crossing the CNP voltage was not observed. Additionally, the photovoltage at CNP did not vanish as in ΔU_{pl}, but showed a negative offset of few μV (Fig. 2(b)), depending on the incoming frequency, as pointed out in Fig. 3. This is not related to the frequency dependence of the source output. Interestingly, a three-time smaller offset was found by rotating the light polarization of 90° at 263 GHz. The origin of this offset can be ascribed to the TE effect. In fact, a thermoelectric voltage (ΔU_{TE}) can be generated by
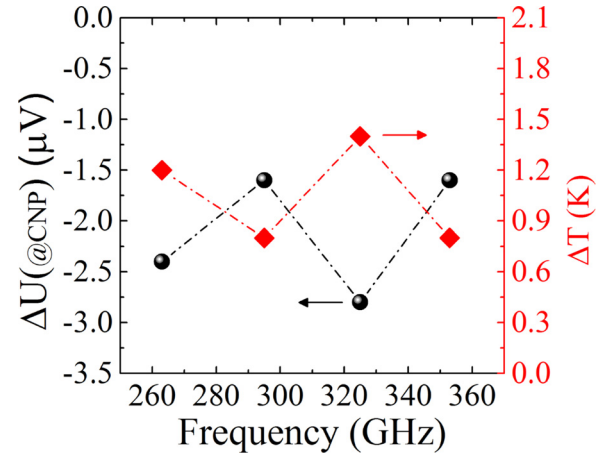

FIG. 3. ΔU at CNP (black dots) and the corresponding estimated temperature difference of the junction (red diamonds) as a function of the radiation frequency. The photovoltages ΔU at CNP are not corrected by the spectral dependence of the source output power.

the presence of carrier density junctions created at the interface of ungated and gated regions.[15,17,39–41] In our detector, p-n/p-p junctions were formed across the FET channel depending on the applied gate bias. Owing to the antenna, the THz radiation is asymmetrically funneled onto the FET channel, inducing a local heating at the junction edge on the source side. In epitaxial graphene an additional TE signal may arise also at the edges of graphene with different thickness, but this contribution is usually dominant only at low temperature (T < RT).[42] The resulting non-equilibrium hot carriers distribution generates a temperature gradient (ΔT) within the channel and thus a thermoelectric voltage $\Delta U_{TE} = (S_1 - S_2)\Delta T$, where $S_{1,2}$ are the thermopowers of the two regions with different carrier density. In order to estimate ΔU_{TE} in our detector, we used Mott's equation, which correlates the thermopower S with the measured electrical conductance σ[43,44] ($\sigma = 1/R_{sd}$, where R_{sd} includes both the contacts and sheet resistance (Fig. 1(c)))

$$S = -\frac{\pi^2 k_B^2 T}{3e}\frac{1}{\sigma}\frac{d\sigma}{dE_F}. \tag{1}$$

Here, k_B is the Boltzmann constant, T is the sample temperature, e is the electron charge, and $E_F = k_B T_F$ is the graphene Fermi energy linked to the Fermi temperature T_F. Independently of the dominant scattering mechanism, Eq. (1) is valid when $T \le 0.2 T_F$[44] or, more in general, when $k_B T \ll E_F$. Generally, it well reproduces the graphene thermopower for RT measured at V_g sufficiently far from V_{CNP},[32] whereas it is valid near the CNP only if the carrier density is such that $k_B T \ll E_F$, like in low mobility graphene as a result of large residual charge fluctuations.[45] In our experiment $T/T_F \sim 0.3$ at CNP, thus a deviation from Mott's formula of less than -30% is predicted both for unscreened charged impurities and short range scattering.[44] A larger deviation ($\sim -50\%$) is expected in the screening conditions.[44,46] Hence, without entering into the details of the dominant scattering mechanism, Eq. (1) was used to roughly estimate the thermopower for gated ($S_g = S(V_g)$) and ungated ($S_{ug} = S(V_g = 0)$) regions and the corresponding $\Delta S = S_g - S_{ug}$. At CNP, $\Delta S \sim -2$ μV/K. Consequently, a ΔT between the
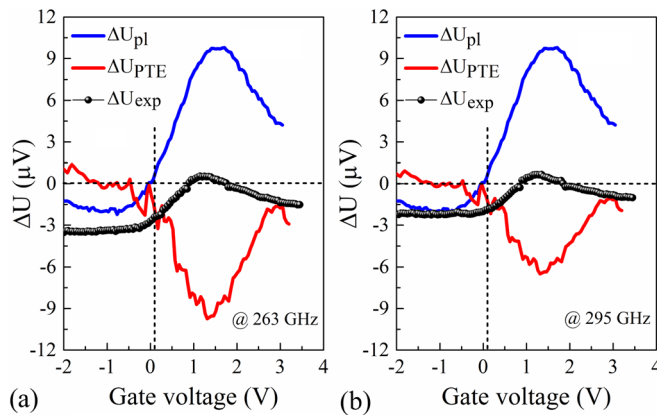
FIG. 4. Calculated plasmonic (blue lines), thermoelectric (red lines), and measured (black dots and lines) photo-induced voltage as a function of the gate voltage at 263 GHz (a) and 295 GHz (b) with $V_{sd} = 0$ mV and parallel polarization. The dashed vertical and horizontal lines indicate the CNP and $\Delta U = 0$ V, respectively.

junctions that ranges between about 0.7 K and 1.5 K, depending on the radiation frequency (Fig. 3), could be accountable for the non-zero photovoltage measured at CNP. Likely, the frequency dependence of ΔT is determined by the sensitivity of the antenna-radiation coupling on the radiation frequency. On the contrary, $\Delta T < 0.5$ K was evaluated when rotating the incident radiation at 90°, further corroborating the relation with the local heating induced by the antenna. Within this scenario, we extracted the thermoelectric voltage ΔU_{TE} as a function of gate bias $\Delta U_{TE}(V_g) = (S_g - S_{ug})\Delta T$. As shown in Figs. 4(a) and 4(b), the calculated thermoelectric response mainly contributes at positive gate voltages and has a curve similar to the plasmonic one but with a opposite sign. Thus, by considering the additional contribution of ΔU_{TE}, the overall behavior of the measured signal ΔU_{exp} could be qualitatively well reproduced. In fact, both the flat and V-shaped behaviors at $V_g < 0$ and $V_g > 0$, respectively, can be explained by the superimposed functional dependence of ΔU_{TE} and ΔU_{pl} on the gate voltage. Moreover, the particular dependence of ΔU_{exp} at positive gate voltages may be used to discriminate the contribution of each mechanism to the total THz detection. In fact, although a more quantitative analysis would require a precise estimation of the C factor in ΔU_{pl} and of the thermopower in ΔU_{TE}, the small sign switch of ΔU_{exp} provides an indication that the plasmonic mechanism was strongly weakened by the thermoelectric effect, although still playing an important role in our detector.

The detector figures of merit were calculated following the procedure in Ref. 16. Therefore, only a lower limit for the responsivity (R) was extracted. The maximum responsivity was achieved at 263 GHz and 325 GHz corresponding to ~0.25 V/W. Instead, R ~ 0.15 V/W was estimated at 295 GHz and 353 GHz. It is worth noting that the maximum responsivity was achieved for the frequencies where the highest temperature gradient was estimated, confirming a more efficient coupling of the THz radiation with the FET channel. Finally, due to the zero-bias configuration, the thermal Johnson-Nyquist noise was assumed as the dominant contribution[15,17] to calculate the NEP. The minimum NEP value was quantified as 80 nW/$\sqrt{Hz}$ and 160 nW/$\sqrt{Hz}$ at 263 GHz/325 GHz and 295 GHz/353 GHz, respectively.

In conclusion, we demonstrated room temperature THz detection with epitaxial graphene grown on silicon carbide as the channel of an antenna-coupled FET. The photoresponse analysis revealed the presence of two competitive independent detection mechanisms: the plasmonic detection due to the electron transport nonlinearity and the thermoelectric effect due to the presence of carrier density junctions and induced temperature gradient across the EGFET channel. Specifically, the analysis of the experimental data suggested that the plasma wave detection might be the dominant mechanism, even though strongly counterbalanced by the thermoelectric response. This detrimental competition resulted in an NEP ~ 80 nW/$\sqrt{Hz}$ and a responsivity of about 0.25 V/W. This is one to two orders of magnitude lower than in plasmonic THz detectors fabricated by exfoliated graphene[16] or CVD graphene transferred on Si/SiO$_2$ substrates,[17] respectively. Improvement of the plasmonic detector performance can be achieved with the maximization of the channel transconductance by minimizing the size of the ungated regions,[17] and thus the associated series resistance, and by using quasi-free standing graphene obtained by hydrogen intercalation.[30] The latter would allow the graphene to be decoupled from the SiC substrate and the electrical properties to be improved,[29] thus enhancing the plasmonic contribution to the photoresponse.[47] Although device improvements are required for a competitive photoresponse, these results demonstrate that epitaxial graphene grown on SiC is a promising candidate for compact, scalable, and fast focal plane detectors for imaging applications.

[1]A. Tredicucci and M. S. Vitiello, IEEE J. Sel. Top. Quantum Electron. 20, 8500109 (2014).
[2]A. C. Ferrari, F. Bonaccorso, V. Falko, K. S. Novoselov, S. Roche, P. Bøggild, S. Borini, F. Koppens, V. Palermo, N. Pugno, J. a. Garrido, R. Sordan, A. Bianco, L. Ballerini, M. Prato, E. Lidorikis, J. Kivioja, C. Marinelli, T. Ryhänen, A. Morpurgo, J. N. Coleman, V. Nicolosi, L. Colombo, A. Fert, M. Garcia-Hernandez, A. Bachtold, G. F. Schneider, F. Guinea, C. Dekker, M. Barbone, C. Galiotis, A. Grigorenko, G. Konstantatos, A. Kis, M. Katsnelson, C. W. J. Beenakker, L. Vandersypen, A. Loiseau, V. Morandi, D. Neumaier, E. Treossi, V. Pellegrini, M. Polini, A. Tredicucci, G. M. Williams, B. H. Hong, J. H. Ahn, J. M. Kim, H. Zirath, B. J. van Wees, H. van der Zant, L. Occhipinti, A. Di Matteo, I. A. Kinloch, T. Seyller, E. Quesnel, X. Feng, K. Teo, N. Rupesinghe, P. Hakonen, S. R. T. Neil, Q. Tannock, T. Löfwander, and J. Kinaret, Nanoscale 7, 4598 (2015).
[3]V. Ryzhii, A. A. Dubinov, V. Otsuji, V. Mitin, and M. S. Shur, J. Appl. Phys. 107, 054505 (2010).
[4]Z. Sun, T. Hasan, F. Torrisi, D. Popa, G. Privitera, F. Wang, F. Bonaccorso, D. M. Basko, and A. C. Ferrari, ACS Nano 4, 803 (2010).
[5]F. Bianco, V. Miseikis, D. Convertino, J.-H. Xu, F. Castellano, H. E. Beere, D. A. Ritchie, M. S. Vitiello, A. Tredicucci, and C. Coletti, Opt. Express 23, 11632 (2015).
[6]A. N. Grigorenko, M. Polini, and K. S. Novoselov, Nat. Photonics 6, 749 (2012).
[7]B. Sensale-Rodriguez, T. Fang, R. Yan, M. M. Kelly, D. Jena, L. Liu, and H. Xing, Appl. Phys. Lett. 99, 113104 (2011).
[8]M. Liu, X. Yin, E. Ulin-Avila, B. Geng, T. Zentgraf, L. Ju, F. Wang, and X. Zhang, Nature 474, 64 (2011).

[9]T. Low and P. Avouris, ACS Nano **8**, 1086 (2014).

[10]F. H. L. Koppens, T. Mueller, P. Avouris, A. C. Ferrari, M. S. Vitiello, and M. Polini, Nat. Nanotechnol. **9**, 780 (2014).

[11]A. V. Muraviev, S. L. Rumyantsev, G. Liu, A. A. Balandin, W. Knap, and M. S. Shur, Appl. Phys. Lett. **103**, 181114 (2013).

[12]M. Mittendorff, S. Winnerl, J. Kamann, J. Eroms, D. Weiss, H. Schneider, and M. Helm, Appl. Phys. Lett. **103**, 021113 (2013).

[13]X. Cai, A. B. Sushkov, R. J. Suess, M. M. Jadidi, G. S. Jenkins, L. O. Nyakiti, R. L. Myers-Ward, S. Li, J. Yan, D. K. Gaskill, T. E. Murphy, H. D. Drew, and M. S. Fuhrer, Nat. Nanotechnol. **9**, 814 (2014).

[14]M. I. Dyakonov and M. S. Shur, IEEE Trans. Electron Devices **43**, 1640 (1996).

[15]L. Vicarelli, M. S. Vitiello, D. Coquillat, A. Lombardo, A. C. Ferrari, W. Knap, M. Polini, V. Pellegrini, and A. Tredicucci, Nat. Mater. **11**, 865 (2012).

[16]D. Spirito, D. Coquillat, S. L. De Bonis, A. Lombardo, M. Bruna, A. C. Ferrari, V. Pellegrini, A. Tredicucci, W. Knap, and M. S. Vitiello, Appl. Phys. Lett. **104**, 061111 (2014).

[17]A. Zak, M. A. Andersson, M. Bauer, J. Matukas, A. Lisauskas, H. G. Roskos, and J. Stake, Nano Lett. **14**, 5834 (2014).

[18]M. Dyakonov, M. Shur, and S. Petersburg, Phys. Rev. Lett. **71**, 2465 (1993).

[19]F. Schuster, D. Coquillat, H. Videlier, M. Sakowicz, F. Teppe, L. Dussopt, B. Giffard, T. Skotnicki, and W. Knap, Opt. Express **19**, 7827 (2011).

[20]W. Li, J. Wang, J. Gou, Z. Huang, and Y. Jiang, J. Infrared Millimeter Terahertz Waves **36**, 42 (2015).

[21]A. W. M. Lee, B. S. Williams, S. Kumar, Q. Hu, and J. L. Reno, IEEE Photonics Technol. Lett. **18**, 1415 (2006).

[22]F. Schwierz, Nat. Nanotechnol. **5**, 487 (2010).

[23]M. Saremi, M. Saremi, H. Niazi, and A. Y. Goharrizi, Superlattices Microstruct. **60**, 67 (2013).

[24]J. Chen, Y. Wen, Y. Guo, B. Wu, L. Huang, Y. Xue, D. Geng, D. Wang, G. Yu, and Y. Liu, J. Am. Chem. Soc. **133**, 17548 (2011).

[25]V. Miseikis, D. Convertino, N. Mishra, M. Gemmi, T. Mashoff, S. Heun, N. Haghighian, F. Bisio, M. Canepa, V. Piazza, and C. Coletti, 2D Mater. **2**, 014006 (2015).

[26]T. Mashoff, D. Convertino, V. Miseikis, C. Coletti, V. Piazza, V. Tozzini, F. Beltram, and S. Heun, Appl. Phys. Lett. **106**, 083901 (2015).

[27]D. S. Lee, C. Riedl, B. Krauss, K. von Klitzing, U. Starke, and J. H. Smet, Nano Lett. **8**(12), 4320–4325 (2008).

[28]C. Coletti, S. Forti, A. Principi, K. V. Emtsev, A. A. Zakharov, K. M. Daniels, B. K. Daas, M. V. S. Chandrashekhar, T. Ouisse, D. Chaussende, A. H. MacDonald, M. Polini, and U. Starke, Phys. Rev. B **88**, 155439 (2013).

[29]E. Pallecchi, F. Lafont, V. Cavaliere, F. Schopfer, D. Mailly, W. Poirier, and A. Ouerghi, Sci. Rep. **4**, 4558 (2014).

[30]C. Riedl, C. Coletti, and U. Starke, J. Phys. D: Appl. Phys. **43**, 374009 (2010).

[31]K. Zou and J. Zhu, Phys. Rev. B **82**, 081407(R) (2010).

[32]S. G. Nam, D. K. Ki, and H. J. Lee, Phys. Rev. B **82**, 245416 (2010).

[33]H. Hibino, S. Tanabe, S. Mizuno, and H. Kageshima, J. Phys. D: Appl. Phys. **45**, 154008 (2012).

[34]C. Yu, Q. Liu, J. Li, W. Lu, Z. He, S. Cai, and Z. Feng, Appl. Phys. Lett. **105**, 183105 (2014).

[35]N. Ray, S. Shallcross, S. Hensel, and O. Pankratov, Phys. Rev. B **86**, 125426 (2012).

[36]S.-H. Ji, J. B. Hannon, R. M. Tromp, V. Perebeinos, J. Tersoff, and F. M. Ross, Nat. Mater. **11**, 114 (2011).

[37]W. Zhu, V. Perebeinos, M. Freitag, and P. Avouris, Phys. Rev. B **80**, 235402 (2009).

[38]A. S. Mayorov, D. C. Elias, M. Mucha-Kruczynski, R. V. Gorbachev, T. Tudorovskiy, A. Zhukov, S. V. Morozov, M. I. Katsnelson, V. I. Fal'ko, A. K. Geim, and K. S. Novoselov, Science **333**, 860 (2011).

[39]M. C. Lemme, F. H. L. Koppens, A. L. Falk, M. S. Rudner, H. Park, L. S. Levitov, and C. M. Marcus, Nano Lett. **11**, 4134 (2011).

[40]N. Gabor, J. Song, Q. Ma, N. Nair, T. Taychatanapat, K. Watanabe, T. Taniguchi, L. S. Levitov, and P. Jarillo-Herrero, Science **334**, 648 (2011).

[41]T. J. Echtermeyer, P. S. Nene, M. Trushin, R. V. Gorbachev, A. L. Eiden, S. Milana, Z. Sun, J. Schliemann, E. Lidorikis, K. S. Novoselov, and A. C. Ferrari, Nano Lett. **14**, 3733 (2014).

[42]J. Park, G. He, R. M. Feenstra, and A. P. Li, Nano Lett. **13**, 3269 (2013).

[43]M. Cutler and N. F. Mott, Phys. Rev. **181**, 1336 (1969).

[44]E. H. Hwang, E. Rossi, and S. Das Sarma, Phys. Rev. B **80**, 235415 (2009).

[45]D. Wang and J. Shi, Phys. Rev. B **83**, 113403 (2011).

[46]X. Wu, Y. Hu, M. Ruan, N. K. Madiomanana, C. Berger, and W. A. De Heer, Appl. Phys. Lett. **99**, 133102 (2011).

[47]A. Tomadin and M. Polini, Phys. Rev. B **88**, 205426 (2013).